

1 **Interpreting Space-Based Trends in Carbon Monoxide**
2 **with Multiple Models**

3
4 Sarah A. Strode^{1,2}, Helen M. Worden³, Megan Damon^{2,4}, Anne R. Douglass², Bryan N.
5 Duncan², Louisa K. Emmons³, Jean-Francois Lamarque³, Michael Manyin^{2,4}, Luke D.
6 Oman², Jose M. Rodriguez², Susan E. Strahan^{1,2}, Simone Tilmes³

7
8 ¹Universities Space Research Association, Columbia, MD, USA

9 ²NASA Goddard Space Flight Center, Greenbelt, MD, USA

10 ³National Center for Atmospheric Research, Boulder, CO, USA

11 ⁴Science Systems and Applications, Inc., Lanham, MD, USA

12
13 *Correspondence to:* S. A. Strode (sarah.a.strode@nasa.gov)

14 **Abstract**

15 We use a series of chemical transport model and chemistry climate model simulations to
16 investigate the observed negative trends in MOPITT CO over several regions of the
17 world, and to examine the consistency of time-dependent emission inventories with
18 observations. We find that simulations driven by the MACCity inventory, used for the
19 Chemistry Climate Modeling Initiative (CCMI), reproduce the negative trends in the CO
20 column observed by MOPITT for 2000-2010 over the eastern United States and Europe.
21 However, the simulations have positive trends over eastern China, in contrast to the
22 negative trends observed by MOPITT. The model bias in CO, after applying MOPITT
23 averaging kernels, contributes to the model-observation discrepancy in the trend over
24 eastern China. This demonstrates that biases in a model's average concentrations can
25 influence the interpretation of the temporal trend compared to satellite observations. The
26 total ozone column plays a role in determining the simulated tropospheric CO trends. A
27 large positive anomaly in the simulated total ozone column in 2010 leads to a negative
28 anomaly in OH and hence a positive anomaly in CO, contributing to the positive trend in
29 simulated CO. These results demonstrate that accurately simulating variability in the
30 ozone column is important for simulating and interpreting trends in CO.

31 **1. Introduction**

33 Carbon monoxide (CO) is an air pollutant that contributes to ozone formation and
34 affects the oxidizing capacity of the troposphere (Thompson, 1992; Crutzen, 1973). Its
35 primary loss is through reaction with OH, which leads to a lifetime of 1-2 months (Bey et
36 al., 2001) and makes CO an excellent tracer of long-range transport. Both fossil fuel
37 combustion and biomass burning are major sources of CO. The biomass burning source
38 shows large interannual variability (van der Werf et al., 2010), while fossil fuel emissions
39 typically change more gradually. The time-dependent MACCity inventory (Granier et
40 al., 2011) shows decreases in CO emissions from the United States and Europe from
41 2000 to 2010 due to increasing pollution controls, but increases in emissions from China.
42 MACCity emissions for years after 2000 are based on the Representative Concentration
43 Pathway (RCP) 8.5 (Riahi et al., 2007). The REAS (Kurokawa et al., 2013) and
44 EDGAR4.2 (EC-JRC/PBL, 2011) inventories also show increasing CO emissions from
45 China. The bottom-up inventory of Zhang et al. (2009) shows an 18% increase in CO
46 emissions from China from 2001 to 2006, and Zhao et al. (2012) estimate a 6% increase
47 between 2005 and 2009. However, there is considerable uncertainty in bottom-up
48 inventories, and comparison of model hindcast simulations driven by bottom-up
49 inventories with observations provides an important test of the time-dependent emission
50 estimates.

51 Space-based observations of CO are now available for over a decade and show
52 trends at both hemispheric and regional scales. Warner et al. (2013) found significant
53 negative trends in both background CO and recently emitted CO at 500 hPa over southern
54 hemisphere oceans and northern hemisphere land and ocean in Atmospheric Infrared
55 Sounder (AIRS) data. Worden et al. (2013) calculated trends in the CO column from
56 several thermal infrared (TIR) instruments including MOPITT and AIRS. They found
57 statistically significant negative trends over Europe, the eastern United States, and China
58 for 2002-2012. He et al. (2013) also report a negative trend in MOPITT near-surface CO
59 over western Maryland.

60 Surface concentrations of CO show downward trends over the United States
61 driven by emission reductions (EPA, 2011), consistent with the space-based trends.
62 Decreases in the partial column of CO from FTIR stations in Europe also show decreases
63 from 1996 to 2006, consistent with emissions decreases (Angelbratt et al., 2011). Yoon

64 and Pozzer (2014) found that a model simulation of 2001 to 2010 reproduced negative
65 trends in surface CO over the eastern U.S. and western Europe, but showed a positive
66 trend in surface CO over southern Asia.

67 The cause of the negative trend over China seen in MOPITT and AIRS data is
68 uncertain. The trend is consistent with the results of Li and Liu (2011), who found
69 decreases in surface CO measurements in Beijing, and with decreases in CO emissions in
70 2008 inferred from the correlation of CO with CO₂ measured at Hateruma Island
71 (Tohjima et al., 2014) and at a rural site in China (Wang et al., 2010). Yumimoto et al.
72 (2014) used inverse modeling of MOPITT data to infer a decrease in CO emissions from
73 China after 2007. The 2008 Olympic Games and the 2009 global economic slowdown
74 led to reductions in CO (Li and Liu, 2011; Worden et al., 2012). However, the negative
75 trend in MOPITT CO is inconsistent with the rising CO emissions of the MACCity and
76 REAS inventories. Inverse modeling of MOPITT version 6 data yields a negative trend
77 in CO emissions from China and a larger global decline in CO emissions than that found
78 in the MACCity inventory (Yin et al., 2015).

79 This study examines whether global hindcast simulations can reproduce the trends
80 and variability in carbon monoxide seen in the MOPITT record. We examine the role of
81 averaging kernels and the contribution of trends at different altitudes to the trends
82 observed by MOPITT. We then examine the impact of OH variability on the simulated
83 trends in CO.

84 **2. Methods**

85 **2.1. MOPITT**

86 The MOPITT instrument onboard the Terra Satellite provides the longest satellite-
87 based record of atmospheric CO, with observations available from March 2000 to
88 present. It provides nearly global coverage every three days (Edwards et al., 2004). We
89 use the monthly Level 3 daytime column data from the Version 5 TIR product, which has
90 negligible drift in the bias over time (Deeter et al., 2013). The level 3 data is a gridded
91 product and includes the a priori and averaging kernel for each grid box. Supplemental
92 Figure S1 shows the MOPITT column averaging kernels averaged over four regions. The
93 column averaging kernels depend on the observed scene, and vary year to year as well as

94 seasonally. The dependence of the column averaging kernels on the CO mixing ratio
95 profile (Deeter, 2009) explains the high values in the lower troposphere over eastern
96 China in winter.

97 We calculate trends and de-seasonalized anomalies for the Eastern U.S., Europe, and
98 eastern China regions described by Worden et al. (2013). Trends that differ from zero by
99 more than the two-sigma uncertainty on the trend are considered statistically significant.
100 We account for autocorrelation of the data for a one-month lag when calculating the
101 uncertainty on the trends. We calculate the annual cycle by fitting the data with a series
102 of sines and cosines as well as the linear trend, and then remove the annual cycle to
103 obtain the de-seasonalized anomalies. Months with no MOPITT data or only a few days
104 of MOPITT data are excluded from the trend analysis. This includes May-August of
105 2001 and August-September of 2009. We report the MOPITT trends for 2000-2010 for
106 comparison with model simulations, and for 2000-2014 to give a longer-term view of the
107 observed trends.

108

109 **2.2. Model Simulations**

110 We use a suite of chemistry climate model (CCM) and chemical transport model
111 (CTM) simulations to interpret the observed trends. The Global Modeling Initiative
112 (GMI) CTM includes both tropospheric (Duncan et al., 2007) and stratospheric (Strahan
113 et al., 2007) chemistry, including over 400 reactions and 124 chemical species.
114 Meteorology for the GMI simulations comes from the Modern-Era Retrospective
115 Analysis for Research and Applications (MERRA) (Rienecker et al., 2011). The GEOS-
116 5 Chemistry Climate Model (GEOSCCM)(Oman et al., 2011) incorporates the GMI
117 chemical mechanism into the GEOS-5 atmospheric general circulation model (AGCM).
118 The GEOSCCM simulations are forced by observed sea surface temperatures (SSTs)
119 from (Reynolds et al., 2002).

120 The Community Earth System Model, CESM1 CAM4-chem, includes 191 chemical
121 tracers and over 400 reactions for both troposphere and stratosphere (Tilmes et al., 2016).
122 The model can be run fully coupled to a free-running ocean, with prescribed SSTs, or
123 with nudged meteorology from GEOS-5 or MERRA analysis. CESM1 CAM4-chem is

124 further coupled to the land model, providing biogenic emissions from the Model of
125 Emissions and Aerosols from Nature (MEGAN), version 2.1 (Guenther et al., 2012).

126 Several simulations were conducted as part of the Chemistry-Climate Model Initiative
127 (CCMI) project (Eyring et al., 2013). These include the Ref-C1 simulation of the
128 GEOSCCM and a Ref-C1 CESM1 CAM4-Chem simulation, hereafter called G-Ref-C1
129 and C-Ref-C1, respectively, and the Ref-C1-SD simulation of the GMI CTM. Both the
130 Ref-C1 and the Ref-C1-SD simulations use time-dependent anthropogenic and biomass
131 burning emissions from the MACCity inventory (Granier et al., 2011), but the Ref-C1-
132 SD simulations use specified meteorology while the Ref-C1 simulations run with
133 prescribed SSTs. The MACCity inventory linearly interpolates the decadal
134 anthropogenic emissions from the ACCMIP inventory (Lamarque et al., 2010) for 2000,
135 and the RCP8.5 emissions for 2005 and 2010, to each year in between. The MACCity
136 biomass burning emissions have year-to-year variability based on the GFED-v2 (van der
137 Werf et al., 2006) inventory. From 2000 to 2010, CO emissions in the MACCity
138 inventory decreased from 31 to 11 Tg yr⁻¹ over the eastern U.S., from 97 to 59 Tg yr⁻¹
139 over Europe, and increased from 56 Tg to 72 Tg yr⁻¹ over eastern China.

140 Given the uncertainty in CO emissions, we conduct a GMI CTM simulation using an
141 alternative time-dependent emissions scenario, called AltEmis. This simulation is
142 described in detail in (Strode et al., 2015b). Briefly, anthropogenic emissions include
143 time-dependence based on EPA (<http://www.epa.gov/ttn/chief/trends/index.html>), the
144 REAS inventory (Ohara et al., 2007), and EMEP
145 (http://www.ceip.at/ms/ceip_home1/ceip_home/webdab_emepdatabase/reported_emissio
146 ndata/), and annual scalings from van Donkelaar et al. (2008). Biomass burning
147 emissions are based on the GFED3 inventory (van der Werf et al., 2010). While the
148 regional emission trends in this simulation are of the same sign as in the Ref-C1 case, the
149 magnitude of the negative trends over the U.S. and Europe are smaller and the positive
150 trend over China is larger, leading to a positive global trend (Fig. 1). We also conduct a
151 sensitivity study called EmFix with anthropogenic and biomass burning emissions held
152 constant at year 2000 levels. Table 1 summarizes the simulations used in this study.

153 We regrid the model output to the MOPITT grid and convolve the simulated CO with
154 the MOPITT averaging kernels and a priori in order to compare the simulated and

155 observed CO columns. The averaging kernels are space and time dependent. We use the
156 following equation from Deeter et al. (2013):

157 $C_{\text{sim}} = C_0 + \mathbf{a}(\mathbf{x}_{\text{mod}} - \mathbf{x}_0)$ (1)

158 where C_{sim} and C_0 are the simulated and a priori CO total columns, respectively, \mathbf{a} is the
159 total column averaging kernel, and \mathbf{x}_{mod} and \mathbf{x}_0 are the modeled and a priori CO profiles,
160 respectively. The column averaging kernel is calculated from the standard averaging
161 kernel matrix, which is based on the log of the CO concentration profile, following the
162 method of Deeter (2009):

163 $a_j = (K / \log_{10}e) \sum \Delta p_i v_{\text{rtv},i} A_{ij}$ (2)

164 where Δp_i and $v_{\text{rtv},i}$ are the pressure thickness and retrieved CO concentration,
165 respectively, of level i , \mathbf{A} is the standard averaging kernel matrix, and $K = 2.12 * 10^{13}$
166 molec cm⁻² hPa⁻¹ ppb⁻¹.

167 We deseasonalize the simulated CO columns and calculate their linear trend
168 following the same procedure that we applied to the MOPITT CO. Months that do not
169 have MOPITT data (June-July 2001 and August-September 2009) are excluded from the
170 analysis of the model trends as well.

171 The Ref-C1 and Ref-C1-SD simulations requested by CCMI extend until 2010.
172 However, the MACCity biomass burning emissions extend only until 2008. CAM4-
173 Chem therefore repeated the biomass burning emissions for 2008 for years 2009-2010.
174 In contrast, the GEOSCCM Ref-C1 and GMI Ref-C1-SD simulations used emissions
175 from GFED3 (van der Werf et al., 2010) for years after 2008. Some simulations were
176 available through 2011, while others ended in 2010. We therefore report results for
177 2000-2010, but note that extending the analysis through 2011 does not alter the
178 conclusions.

179 **3. Results**

180 **3.1. Trends over Europe, the United States, and the Northern Hemisphere**

181 The hindcast simulations driven by MACCity emissions (G-Ref-C1, Ref-C1-SD, and
182 C-Ref-C1) show negative trends in CO over the U.S. and Europe that agree with the
183 observed slope from MOPITT within the uncertainty (Fig. 2, Table 2). The MOPITT

184 trends for both regions are statistically significant for both regions, as shown by Worden
185 et al. (2013). These results are consistent with the findings of Yin et al. (2015), whose
186 inversion of MOPITT data showed a posteriori trends in CO emissions over the U.S. and
187 western Europe that were consistent with but slightly larger than the a priori trends. The
188 EmFix hindcast shows a positive, though non-significant, trend for both regions,
189 indicating that the decrease in CO emissions is necessary for reproducing the downward
190 trend in the CO column. The AltEmis simulation fails to produce the negative trends,
191 despite including negative trends in regional emissions for both the U.S. and Europe.
192 The impact of these negative regional trends is insufficient to overcome the positive
193 global emission trend in the AltEmis scenario (Fig. 1), leading to positive trends in CO.

194 Figure 2 also reveals a negative bias in the simulated CO column between the models
195 and MOPITT. A low bias in simulated CO at northern latitudes is often present in global
196 models (Naik et al., 2013), and may indicate a high bias in northern hemisphere OH
197 (Strode et al., 2015a) or CO dry deposition (Stein et al., 2014), as well as an
198 underestimate of CO emissions.

199 The deseasonalized anomalies in the MOPITT and simulated CO columns are shown
200 in Fig. 2b,d, and the correlation coefficient between the observed and simulated monthly
201 anomalies are presented in Table 2b. The highest correlations are for the AltEmis and
202 Ref-C1-SD simulations of the GMI CTM. This result is consistent with the use of year-
203 specific meteorology, which we expect to better match the transport of particular years.
204 The lowest correlations are for the EmFix simulation. This is expected since the EmFix
205 simulation does not include inter-annual variability (IAV) in biomass burning. The IAV
206 in biomass burning makes a large contribution to the IAV of CO (Voulgarakis et al.,
207 2015).

208 The role of biomass burning in driving the CO variability is even more evident at the
209 hemispheric scale. Figure 2g,h shows the anomalies in MOPITT and the simulations for
210 the northern hemisphere (0-60N). The EmFix simulation shows almost no correlation,
211 while the other simulations have correlation coefficients exceeding 0.6 (Table 2). The
212 role of changing anthropogenic emissions is also evident, as the Ref-C1-SD simulation
213 captures the 2008-2009 dip in the CO column while the EmFix simulation does not.
214 Gratz et al. (2015) found decreasing CO concentrations at Mount Bachelor Observatory

215 in Oregon during spring for 2004-2013, which they attribute to reductions in emissions
216 leading to a lower hemispheric background. We also note that Ref-C1-SD and G-Ref-
217 C1 have similar correlations with the observed variability for the northern hemisphere
218 (Table 2), indicating that transport differences are less important for variability at the
219 hemispheric scale.

220 **3.2. Trend over China**

221 Observations from MOPITT show a negative trend in the CO column over eastern
222 China for 2002-2012 (Worden et al., 2013). The negative trend for the years 2000-2014
223 exceeds that for 2000-2010 (Table 2), showing that it is not driven solely by temporary
224 emission reductions in 2008. Our simulations do not reproduce this trend, and instead
225 show increases in the CO column (Fig. 2e), which is expected given that CO emissions
226 from China increase in four of the five simulations. The anomalies (Fig. 2f) show that
227 the discrepancy in the simulated versus observed trends is driven largely by the failure of
228 the simulations to capture the 2008 dip in the CO column, leading to an overestimate that
229 continues through 2010. This suggests emission reductions in China during this time
230 period are not adequately captured by the emission inventories. However, the good
231 agreement between the observed and simulated decreases in CO for the northern
232 hemisphere as a whole (Fig. 2g,h) suggest that on a global scale, the emission time series
233 is reasonable. Consequently, we examine several other factors that may contribute to the
234 difference in sign between the MOPITT and simulated CO trends.

235 Regional trends in CO are expected to vary with altitude, with surface concentrations
236 most heavily influenced by local emissions. MOPITT TIR retrievals have higher
237 sensitivity to CO in the mid-troposphere than at the surface (Deeter et al., 2004), so the
238 trend in the MOPITT CO column will be weighted towards the trends in free tropospheric
239 CO rather than near-surface CO. We quantify this impact on our Ref-C1-SD CO column
240 trends by comparing the trend in the pure-model CO column with that of the simulated
241 column convolved with the MOPITT averaging kernels.

242 The simulated CO trend over eastern China for 2000-2010 is positive (but not
243 significant) both with and without the averaging kernels, but application of the MOPITT
244 kernels increases the positive trend from $1.3*10^{16}$ molec $\text{cm}^{-2} \text{ yr}^{-1}$ to $1.4*10^{16}$ molec cm^{-2}
245 yr^{-1} . This result is initially surprising since we expect trends in the mid-troposphere to be

246 more strongly influenced by the decrease in the hemispheric CO background. Indeed, the
247 trends in CO concentration over eastern China simulated in Ref-C1-SD switch from
248 positive in the lower troposphere to negative in the middle and upper troposphere.
249 However, the application of the kernels results in more positive (or less negative) trends
250 in all regions.

251 Yoon et al. (2013) show that since the averaging kernels vary over time, a bias
252 between the true atmosphere and the a priori assumed by MOPITT can lead to an
253 artificial trend in the retrieved CO. Similarly, the bias between the average simulated CO
254 concentrations and the MOPITT a priori, evident in Figure 2, can lead to an artifact in the
255 simulated CO trend when the simulation is convolved with the MOPITT averaging
256 kernels. This is due to the changing contribution of the a priori when the vertical
257 sensitivity (averaging kernel) is varying in time. MOPITT vertical sensitivity varies with
258 time due to instrument degradation as well as the change in CO abundance. The bias in
259 CO varies with altitude, so if the vertical sensitivity described by the averaging kernel
260 changes, this will change the value of the convolved CO column even if there were no
261 changes in the CO profile. Furthermore, changes in the averaging kernel result in more
262 or less weight placed on the a priori versus the CO simulated by the model. Thus, a
263 difference between the a priori and the model means that placing more (or less) weight on
264 the a priori will change the resulting value of C_{sim} . Since the a priori profiles and
265 columns are constant in time, taking the time derivative of equation 1 yields:

$$266 \quad \partial C_{\text{sim}} / \partial t = \mathbf{a} (\partial \mathbf{x}_{\text{mod}} / \partial t) + \partial \mathbf{a} / \partial t (\mathbf{x}_{\text{mod}} - \mathbf{x}_0) \quad (3)$$

267 The second term on the right hand side shows that the larger the bias between the
268 modeled CO and the a priori, the larger the impact of the changing averaging kernel.

269 We quantify this effect by convolving the simulated CO for each year with the
270 MOPITT averaging kernels for the year 2008, thus removing the effect of the time-
271 dependence of the averaging kernels. The resulting trend, 0.56×10^{16} molec $\text{cm}^{-2} \text{ yr}^{-1}$, is
272 less positive than the pure model trend or the original simulated trend. Thus, accounting
273 for the time-dependence of the averaging kernels convolved with model bias reduces but
274 does not eliminate the discrepancy with the observed trend. Comparing the trend for the
275 constant averaging kernel case with the original simulated trend for Ref-C1-SD (1.4×10^{16}
276 molec $\text{cm}^{-2} \text{ yr}^{-1}$) suggests that the changing averaging kernels combined with the model

277 bias contribute 0.84×10^{16} molec $\text{cm}^{-2} \text{ yr}^{-1}$ to the simulated trend. Other regions also show
278 a more negative trend when the same averaging kernel is applied to the model results for
279 all years. The large bias in CO at middle and high northern latitudes commonly seen in
280 modeling studies thus impacts the ability of models to reproduce and attribute observed
281 trends in satellite data.

282 Figure 2 and Table 2 also show a positive trend in the GMI EmFix simulation for
283 eastern China. This larger trend in the EmFix simulation than the Ref-C1-SD simulation
284 indicates that the net decrease in emissions contributes to decreasing CO over eastern
285 China, consistent with the observed negative trend, but other factors in the model cause
286 an increase in CO over eastern China even when all emissions are constant. Subtracting
287 the EmFix trend from the Ref-C1-SD trend shows that the changing emissions contribute
288 a CO trend of -0.7 molec $\text{cm}^{-2} \text{ yr}^{-1}$ over eastern China. The 2.1 molec $\text{cm}^{-2} \text{ yr}^{-1}$ trend in the
289 EmFix simulation, which reflects the impacts of the simulated chemistry and transport,
290 thus contributes to the erroneous sign of the trend in the GMI simulations. The trends in
291 the EmFix simulation for the northern hemisphere average and the eastern U.S. and
292 Europe are positive as well (Table 2). We examine their cause in the next section.

293 3.3. Contribution of OH Interannual Variability

294

295 Since the EmFix simulation shows a positive trend in the northern hemisphere, we
296 next examine the variability in the CO sink, OH. We also examine variability in the total
297 ozone column, since overhead ozone is a major driver of OH variability (Duncan and
298 Logan, 2008). Figure 3 shows the variability in CO and OH in the EmFix simulation.
299 The positive and negative anomalies in CO correspond with the negative and positive
300 anomalies, respectively, in OH. The anomalies in OH are in turn inversely related to
301 anomalies in the total ozone column. The correlation coefficient between OH and
302 column ozone is -0.53 for the 15°S - 15°N average, -0.72 for the 15° - 25°N average, and $-$
303 0.75 for the 30° - 60°N average. The large NH ozone anomaly in 2010, in particular, leads
304 to a large anomaly in OH and thus CO. This OH anomaly extends from the northern
305 tropics to the midlatitudes. The large CO anomaly near the end of the time series
306 contributes to the apparent 11-year trend. We note that since the lifetime of CO is several

307 months, CO anomalies are not expected to have a one-to-one correspondence with the
308 OH anomalies.

309 The large anomaly in the simulated total ozone column in 2010 is overestimated
310 compared to observations. Figure 4 shows the time-dependence of the total ozone
311 column from 30°-60°N in EmFix compared to SBUV data (Frith et al., 2014). While the
312 observations show an anomaly in 2010, the magnitude is smaller than that produced by
313 the simulation. Steinbrecht et al. (2011) attribute the 2010 anomaly in northern
314 midlatitude ozone observations to a combination of an unusually strong negative Arctic
315 Oscillation and North Atlantic Oscillation and the easterly phase of the quasi-biennial
316 oscillation.

317 While the impact of OH interannual variability on the apparent trend in CO is clear in
318 the EmFix simulation, this source of variability is partially masked by large interannual
319 variability in CO emissions in the other simulations. We examine the correlation
320 between the de-trended and deseasonalized CO anomalies from 10°S-10°N in the Ref-
321 C1-SD simulation and the CO emissions as well as the simulated OH and column ozone.
322 Since the CO emitted in a given month can influence concentrations for several
323 subsequent months, we use a 3-month smoothing of the emission time series. We find a
324 high correlation ($r=0.88$) between the CO anomalies and the CO emissions. This
325 correlation is also evident in the MOPITT data, as the MOPITT CO anomalies have a
326 correlation of $r=0.70$ with the emissions. Figure 5 shows the strong relationship between
327 the simulated CO anomalies and the CO emissions. However, the colors in Fig. 5
328 indicate that the scatter for a given level of emissions is often linked to the OH
329 anomalies, with low/high OH anomalies leading to CO that is higher/lower than would be
330 predicted just from the CO emissions. We find that the 10°S-10°N OH in the Ref-C1-SD
331 simulation is anticorrelated with CO ($r=-0.62$) and with the total ozone column ($r=-0.68$).
332 Consequently, the simulated ozone column plays a role in modulating tropical CO
333 variability even when variable CO emissions are included, although the emissions still
334 play the strongest role.

335 **4. Conclusions**

336 We conducted a series of multi-year simulations to analyze the causes of the negative
337 trends in MOPITT CO reported by Worden et al. (2013). Both CTM and CCM
338 simulations driven by the MACCity emissions reproduce the observed trends over the
339 eastern U.S. and Europe, providing confidence in the regional emission trends.

340 None of the simulations reproduce the observed negative trend over eastern China.
341 This negative trend persists even with the MOPITT data extended out to 2014. The
342 MOPITT averaging kernels are weighted towards the free troposphere, where the relative
343 importance of hemispheric versus local trends is greater. However, our simulations
344 indicate that this effect is insufficient to explain the negative trends over China. Indeed,
345 the negative trend in MOPITT CO over eastern China (-2.9×10^{16} molec $\text{cm}^{-2} \text{ yr}^{-1}$) is
346 stronger than that of the northern hemisphere average (-1.4×10^{16} molec $\text{cm}^{-2} \text{ yr}^{-1}$),
347 indicating that changes in hemispheric CO account for less than half of the trend over
348 China. While the simulations' underestimate of the observed trend likely indicates a too
349 positive emission trend for China, several other factors play a role in the model-
350 observation mismatch. We find that the time-dependent MOPITT averaging kernels,
351 combined with the low bias in simulated CO, provides a positive component to the
352 simulated trends. Large anomalies in the simulated ozone column in the GMI CTM
353 simulations also contribute a positive component to the northern hemisphere trends due to
354 their impact on OH. For the Ref-C1-SD simulation, the trends due to the model bias
355 combined with changing averaging kernels (0.84×10^{16} molec $\text{cm}^{-2} \text{ yr}^{-1}$) and to the
356 simulated chemistry and transport (2.1×10^{16} molec $\text{cm}^{-2} \text{ yr}^{-1}$) can together account for
357 almost 70% of the 4.3×10^{16} molec $\text{cm}^{-2} \text{ yr}^{-1}$ difference between the Ref-C1-SD and
358 MOPITT trends over eastern China.

359 Variability in emissions is the primary driver of year-to-year variability in simulated
360 CO, but OH variability also plays a role. The simulated OH is anti-correlated with both
361 CO and the total ozone column, highlighting the importance of realistic overhead ozone
362 columns for accurately simulating CO variability and trends. In addition, further work is
363 needed to understand recent changes in CO emissions from China.

364

365 **Acknowledgements**

366 This work was supported by NASA's Modeling, Analysis, and Prediction program
367 and computing resources from the NASA High-End Computing Program. We thank
368 Bruce Van Aartsen for contributing to the GMI simulations. The CESM project is
369 supported by the National Science Foundation and the Office of Science (BER) of the US
370 Department of Energy. The MOPITT project is supported by the NASA Earth Observing
371 System (EOS) Program. The National Center for Atmospheric Research (NCAR) is
372 sponsored by the National Science Foundation.

373

374
375 Angelbratt, J., Mellqvist, J., Simpson, D., Jonson, J., Blumenstock, T., Borsdorff, T.,
376 Duchatelet, P., Forster, F., Hase, F., Mahieu, E., De Maziere, M., Notholt, J., Petersen,
377 A., Raffalski, U., Servais, C., Sussmann, R., Warneke, T., and Vigouroux, C.: Carbon
378 monoxide (CO) and ethane (C₂H₆) trends from ground-based solar FTIR measurements
379 at six European stations, comparison and sensitivity analysis with the EMEP model,
380 Atmospheric Chemistry and Physics, 11, 9253-9269, 10.5194/acp-11-9253-2011, 2011.
381 Bey, I., Jacob, D., Logan, J., and Yantosca, R.: Asian chemical outflow to the Pacific in
382 spring: Origins, pathways, and budgets, Journal of Geophysical Research-Atmospheres,
383 106, 23097-23113, 10.1029/2001JD000806, 2001.
384 Crutzen, P.: A Discussion of the Chemistry of Some Minor Constituents in the
385 Stratosphere and Troposphere, Pure and Applied Geophysics, 106, 1385-1399,
386 10.1007/BF00881092, 1973.
387 Deeter, M., Emmons, L., Edwards, D., Gille, J., and Drummond, J.: Vertical resolution
388 and information content of CO profiles retrieved by MOPITT, Geophysical Research
389 Letters, 31, 10.1029/2004GL020235, 2004.
390 Deeter, M. N.: MOPITT (Measurements of Pollution in the Troposphere) Validated
391 Version 4 Product User's Guide, National Center for Atmospheric Research. Available
392 at http://web3.acd.ucar.edu/mopitt/v4_users_guide_val.pdf, 2009.
393 Deeter, M. N., Martinez-Alonso, S., Edwards, D. P., Emmons, L. K., Gille, J. C.,
394 Worden, H. M., Pittman, J. V., Daube, B. C., and Wofsy, S. C.: Validation of MOPITT
395 Version 5 thermal-infrared, near-infrared, and multispectral carbon monoxide profile
396 retrievals for 2000-2011, Journal of Geophysical Research-Atmospheres, 118, 6710-
397 6725, 10.1002/jgrd.50272, 2013.
398 Duncan, B. N., Strahan, S. E., Yoshida, Y., Steenrod, S. D., and Livesey, N.: Model study
399 of the cross-tropopause transport of biomass burning pollution, Atmospheric Chemistry
400 and Physics, 7, 3713-3736, 2007.
401 Duncan, B. N., and Logan, J. A.: Model analysis of the factors regulating the trends and
402 variability of carbon monoxide between 1988 and 1997, Atmospheric Chemistry and
403 Physics, 8, 7389-7403, 2008.
404 Edwards, D. P., Emmons, L. K., Hauglustaine, D. A., Chu, D. A., Gille, J. C., Kaufman,
405 Y. J., Petron, G., Yurganov, L. N., Giglio, L., Deeter, M. N., Yudin, V., Ziskin, D. C.,
406 Warner, J., Lamarque, J. F., Francis, G. L., Ho, S. P., Mao, D., Chen, J., Grechko, E. I.,
407 and Drummond, J. R.: Observations of carbon monoxide and aerosols from the Terra

408 satellite: Northern Hemisphere variability, *Journal of Geophysical Research-
409 Atmospheres*, 109, 10.1029/2004jd004727, 2004.

410 EPA: Our Nation's Air - Status and Trends through 2010, edited by: EPA-454/R-12-001,
411 Research Triangle Park, NC, 2011.

412 Eyring, V., Lamarque, J.-F., Hess, P., Arfeuille, F., Bowman, K., Chipperfield, M. P.,
413 Duncan, B., Fiore, A., Gettelman, A., and Giorgetta, M. A.: Overview of IGAC/SPARC
414 Chemistry-Climate Model Initiative (CCMI) community simulations in support of
415 upcoming ozone and climate assessments, *Sparc Newsletter*, 40, 48-66, 2013.

416 Frith, S., Kramarova, N., Stolarski, R., McPeters, R., Bhartia, P., and Labow, G.: Recent
417 changes in total column ozone based on the SBUV Version 8.6 Merged Ozone Data Set,
418 *Journal of Geophysical Research: Atmospheres*, 119, 9735-9751, 2014.

419 Granier, C., Bessagnet, B., Bond, T., D'Angiola, A., van der Gon, H. D., Frost, G. J.,
420 Heil, A., Kaiser, J. W., Kinne, S., Klimont, Z., Kloster, S., Lamarque, J. F., Liousse, C.,
421 Masui, T., Meleux, F., Mieville, A., Ohara, T., Raut, J. C., Riahi, K., Schultz, M. G.,
422 Smith, S. J., Thompson, A., van Aardenne, J., van der Werf, G. R., and van Vuuren, D.
423 P.: Evolution of anthropogenic and biomass burning emissions of air pollutants at global
424 and regional scales during the 1980-2010 period, *Climatic Change*, 109, 163-190,
425 10.1007/s10584-011-0154-1, 2011.

426 Gratz, L., Jaffe, D., and Hee, J.: Causes of increasing ozone and decreasing carbon
427 monoxide in springtime at the Mt. Bachelor Observatory from 2004 to 2013,
428 *Atmospheric Environment*, 109, 323-330, 10.1016/j.atmosenv.2014.05.076, 2015.

429 Guenther, A., Jiang, X., Heald, C., Sakulyanontvittaya, T., Duhl, T., Emmons, L., and
430 Wang, X.: The Model of Emissions of Gases and Aerosols from Nature version 2.1
431 (MEGAN2. 1): an extended and updated framework for modeling biogenic emissions,
432 2012.

433 He, H., Stehr, J., Hains, J., Krask, D., Doddridge, B., Vinnikov, K., Carty, T., Hosley, K.,
434 Salawitch, R., and Worden, H.: Trends in emissions and concentrations of air pollutants
435 in the lower troposphere in the Baltimore/Washington airshed from 1997 to 2011,
436 *Atmospheric Chemistry and Physics*, 13, 7859-7874, 2013.

437 Kurokawa, J., Ohara, T., Morikawa, T., Hanayama, S., Janssens-Maenhout, G., Fukui, T.,
438 Kawashima, K., and Akimoto, H.: Emissions of air pollutants and greenhouse gases over
439 Asian regions during 2000-2008: Regional Emission inventory in ASia (REAS) version
440 2, *Atmospheric Chemistry and Physics*, 13, 11019-11058, 10.5194/acp-13-11019-2013,
441 2013.

442 Lamarque, J.F., Bond, T.C., Eyring, V., Granier, C., Heil, A., Klimont, Z., Lee, D.,
443 Liousse, C., Mieville, A., Owen, B. and Schultz, M.G.: Historical (1850–2000) gridded
444 anthropogenic and biomass burning emissions of reactive gases and aerosols:
445 methodology and application, *Atmospheric Chemistry and Physics*, 10, 7017-7039, 2010.

446 Li, L., and Liu, Y.: Space-borne and ground observations of the characteristics of CO
447 pollution in Beijing, 2000–2010, *Atmospheric Environment*, 45, 2367-2372,
448 <http://dx.doi.org/10.1016/j.atmosenv.2011.02.026>, 2011.

449 Naik, V., Voulgarakis, A., Fiore, A. M., Horowitz, L. W., Lamarque, J. F., Lin, M.,
450 Prather, M. J., Young, P. J., Bergmann, D., Cameron-Smith, P. J., Cionni, I., Collins, W.
451 J., Dalsoren, S. B., Doherty, R., Eyring, V., Faluvegi, G., Folberth, G. A., Josse, B., Lee,
452 Y. H., MacKenzie, I. A., Nagashima, T., van Noije, T. P. C., Plummer, D. A., Righi, M.,
453 Rumbold, S. T., Skeie, R., Shindell, D. T., Stevenson, D. S., Strode, S., Sudo, K., Szopa,

454 S., and Zeng, G.: Preindustrial to present-day changes in tropospheric hydroxyl radical
455 and methane lifetime from the Atmospheric Chemistry and Climate Model
456 Intercomparison Project (ACCMIP), *Atmospheric Chemistry and Physics*, 13, 5277-
457 5298, 10.5194/acp-13-5277-2013, 2013.

458 Ohara, T., Akimoto, H., Kurokawa, J., Horii, N., Yamaji, K., Yan, X., and Hayasaka, T.:
459 An Asian emission inventory of anthropogenic emission sources for the period 1980-
460 2020, *Atmospheric Chemistry and Physics*, 7, 4419-4444, 2007.

461 Oman, L. D., Ziemke, J. R., Douglass, A. R., Waugh, D. W., Lang, C., Rodriguez, J. M.,
462 and Nielsen, J. E.: The response of tropical tropospheric ozone to ENSO, *Geophysical
463 Research Letters*, 38, 10.1029/2011gl047865, 2011.

464 Reynolds, R., Rayner, N., Smith, T., Stokes, D., and Wang, W.: An improved in situ and
465 satellite SST analysis for climate, *Journal of Climate*, 15, 1609-1625, 10.1175/1520-
466 0442(2002)015<1609:AIISAS>2.0.CO;2, 2002.

467 Riahi, K., Grübler, A., and Nakicenovic, N.: Scenarios of long-term socio-economic and
468 environmental development under climate stabilization, *Technological Forecasting and
469 Social Change*, 74, 887-935, 2007.

470 Riener, M. M., Suarez, M. J., Gelaro, R., Todling, R., Bacmeister, J., Liu, E.,
471 Babilovich, M. G., Schubert, S. D., Takacs, L., Kim, G.-K., Bloom, S., Chen, J., Collins,
472 D., Conaty, A., da Silva, A., Gu, W., Joiner, J., Koster, R. D., Lucchesi, R., Molod, A.,
473 Owens, T., Pawson, S., Pégion, P., Redder, C. R., Reichle, R., Robertson, F. R., Ruddick,
474 A. G., Sienkiewicz, M., and Woollen, J.: MERRA: NASA's Modern-Era Retrospective
475 Analysis for Research and Applications, *Journal of Climate*, 24, 3624-3648,
476 10.1175/JCLI-D-11-00015.1, 2011.

477 Stein, O., Schultz, M., Bouarar, I., Clark, H., Huijnen, V., Gaudel, A., George, M., and
478 Clerbaux, C.: On the wintertime low bias of Northern Hemisphere carbon monoxide
479 found in global model simulations, *Atmospheric Chemistry and Physics*, 14, 9295-9316,
480 10.5194/acp-14-9295-2014, 2014.

481 Steinbrecht, W., Köhler, U., Claude, H., Weber, M., Burrows, J.P., and van der A, R.J.:
482 Very high ozone columns at northern mid-latitudes in 2010, *Geophysical Research
483 Letters*, 38, 10.1029/2010GL046634, 2011.

484 Strahan, S. E., Duncan, B. N., and Hoor, P.: Observationally derived transport diagnostics
485 for the lowermost stratosphere and their application to the GMI chemistry and transport
486 model, *Atmospheric Chemistry and Physics*, 7, 2435-2445, 2007.

487 Strode, S., Duncan, B., Yegorova, E., Kouatchou, J., Ziemke, J., and Douglass, A.:
488 Implications of carbon monoxide bias for methane lifetime and atmospheric composition
489 in chemistry climate models, *Atmospheric Chemistry and Physics*, 15, 11789-11805,
490 2015a.

491 Strode, S. A., Rodriguez, J. M., Logan, J. A., Cooper, O. R., Witte, J. C., Lamsal, L. N.,
492 Damon, M., Van Aartsen, B., Steenrod, S. D., and Strahan, S. E.: Trends and variability
493 in surface ozone over the United States, *Journal of Geophysical Research: Atmospheres*,
494 120, 9020-9042, 2015b.

495 Thompson, A.: The Oxidizing Capacity of the Earth's Atmosphere: Probable Past and
496 Future Change, *Science*, 256, 1157-1165, 10.1126/science.256.5060.1157, 1992.

497 Tilmes, S., Lamarque, J. F., Emmons, L. K., Kinnison, D. E., Marsh, D., Garcia, R. R.,
498 Smith, A. K., Neely, R. R., Conley, A., Vitt, F., Val Martin, M., Tanimoto, H., Simpson,
499 I., Blake, D. R., and Blake, N.: Representation of the Community Earth System Model

500 (CESM1) CAM4-chem within the Chemistry-ClimateModel Initiative (CCMI), Geosci.
501 Model Dev. Discuss., 2016, 1-50, 10.5194/gmd-2015-237, 2016.

502 Tohjima, Y., Kubo, M., Minejima, C., Mukai, H., Tanimoto, H., Ganshin, A.,
503 Maksyutov, S., Katsumata, K., Machida, T., and Kita, K.: Temporal changes in the
504 emissions of CH₄ and CO from China estimated from CH₄/CO₂ and CO/CO₂
505 correlations observed at Hateruma Island, Atmospheric Chemistry and Physics, 14, 1663-
506 1677, 10.5194/acp-14-1663-2014, 2014.

507 van der Werf, G. R., Randerson, J. T., Giglio, L., Collatz, G. J., Kasibhatla, P.S., and
508 Arellano, Jr., A.F.: Interannual variability in global biomass burning emissions from
509 1997-2004, Atmospheric Chemistry and Physics, 6, 3423-3441, 2006.

510 van der Werf, G. R., Randerson, J. T., Giglio, L., Collatz, G. J., Mu, M., Kasibhatla, P.
511 S., Morton, D. C., DeFries, R. S., Jin, Y., and van Leeuwen, T. T.: Global fire emissions
512 and the contribution of deforestation, savanna, forest, agricultural, and peat fires (1997-
513 2009), Atmospheric Chemistry and Physics, 10, 11707-11735, 10.5194/acp-10-11707-
514 2010, 2010.

515 van Donkelaar, A., Martin, R. V., Leaitch, W. R., Macdonald, A. M., Walker, T. W.,
516 Streets, D. G., Zhang, Q., Dunlea, E. J., Jimenez, J. L., Dibb, J. E., Huey, L. G., Weber,
517 R., and Andreae, M. O.: Analysis of aircraft and satellite measurements from the
518 Intercontinental Chemical Transport Experiment (INTEX-B) to quantify long-range
519 transport of East Asian sulfur to Canada, Atmospheric Chemistry and Physics, 8, 2999-
520 3014, 2008.

521 Voulgarakis, A., Marlier, M., Faluvegi, G., Shindell, D., Tsigaridis, K., and Mangeon, S.:
522 Interannual variability of tropospheric trace gases and aerosols: The role of biomass
523 burning emissions, Journal of Geophysical Research-Atmospheres, 120, 7157-7173,
524 10.1002/2014JD022926, 2015.

525 Wang, Y., Munger, J., Xu, S., McElroy, M., Hao, J., Nielsen, C., and Ma, H.: CO₂ and its
526 correlation with CO at a rural site near Beijing: implications for combustion efficiency in
527 China, Atmospheric Chemistry and Physics, 10, 8881-8897, 10.5194/acp-10-8881-2010,
528 2010.

529 Warner, J., Carminati, F., Wei, Z., Lahoz, W., and Attie, J.: Tropospheric carbon
530 monoxide variability from AIRS under clear and cloudy conditions, Atmospheric
531 Chemistry and Physics, 13, 12469-12479, 10.5194/acp-13-12469-2013, 2013.

532 Worden, H. M., Cheng, Y., Pfister, G., Carmichael, G. R., Zhang, Q., Streets, D. G.,
533 Deeter, M., Edwards, D. P., Gille, J. C., and Worden, J. R.: Satellite-based estimates of
534 reduced CO and CO₂ emissions due to traffic restrictions during the 2008 Beijing
535 Olympics, Geophysical Research Letters, 39, 2012.

536 Worden, H. M., Deeter, M. N., Frankenberg, C., George, M., Nichitiu, F., Worden, J.,
537 Aben, I., Bowman, K. W., Clerbaux, C., Coheur, P. F., de Laat, A. T. J., Detweiler, R.,
538 Drummond, J. R., Edwards, D. P., Gille, J. C., Hurtmans, D., Luo, M., Martinez-Alonso,
539 S., Massie, S., Pfister, G., and Warner, J. X.: Decadal record of satellite carbon monoxide
540 observations, Atmospheric Chemistry and Physics, 13, 837-850, 10.5194/acp-13-837-
541 2013, 2013.

542 Yin, Y., Chevallier, F., Ciais, P., Broquet, G., Fortems-Cheiney, A., Pison, I., and
543 Saunois, M.: Decadal trends in global CO emissions as seen by MOPITT, Atmos. Chem.
544 Phys., 15, 13433-13451, 10.5194/acp-15-13433-2015, 2015.

545 Yoon, J., Pozzer, A., Hoor, P., Chang, D., Beirle, S., Wagner, T., Schloegl, S., Lelieveld,
546 J., and Worden, H.: Technical Note: Temporal change in averaging kernels as a source of
547 uncertainty in trend estimates of carbon monoxide retrieved from MOPITT, Atmospheric
548 Chemistry and Physics, 13, 11307-11316, 10.5194/acp-13-11307-2013, 2013.
549 Yoon, J., and Pozzer, A.: Model-simulated trend of surface carbon monoxide for the
550 2001-2010 decade, Atmospheric Chemistry and Physics, 14, 10465-10482, 10.5194/acp-
551 14-10465-2014, 2014.
552 Yumimoto, K., Uno, I., and Itahashi, S.: Long-term inverse modeling of Chinese CO
553 emission from satellite observations, Environmental Pollution, 195, 308-318,
554 10.1016/j.envpol.2014.07.026, 2014.
555 Zhang, Q., Streets, D. G., Carmichael, G. R., He, K. B., Huo, H., Kannari, A., Klimont,
556 Z., Park, I. S., Reddy, S., Fu, J. S., Chen, D., Duan, L., Lei, Y., Wang, L. T., and Yao, Z.
557 L.: Asian emissions in 2006 for the NASA INTEX-B mission, Atmospheric Chemistry
558 and Physics, 9, 5131-5153, 2009.
559 Zhao, Y., Nielsen, C. P., McElroy, M. B., Zhang, L., and Zhang, J.: CO emissions in
560 China: Uncertainties and implications of improved energy efficiency and emission
561 control, Atmospheric Environment, 49, 103-113, 10.1016/j.atmosenv.2011.12.015, 2012.
562

563

Table 1: Description of Simulations

Simulation	Model	Meteorology	Anthropogenic Emissions	Biomass Burning Emissions
G-Ref-C1	GEOSCC M	internally derived	MACCity	MACCity, GFED3 (2009-2010)
C-Ref-C1	CAM4-Chem	internally derived	MACCity	MACCity, then repeat 2008
Ref-C1-SD	GMI	MERRA	MACCity	Same as GEOSCCM
EmFix	GMI	MERRA	Fixed at 2000	Fixed at 2000
AltEmis	GMI	MERRA	Strode et al [2015]	GFED3

Table 2: Regional Trends and Correlations

a. Trends^{1,2}

	Years	E. USA	Europe	E. China	N. Hemisphere
G-Ref-C1 ³	2000-2010	-2.2 (0.38)	-1.8 (0.42)	2.2 (1.1)	-0.76 (3.0)
C-Ref-C1 ³	2000-2010	-3.4 (0.54)	-2.9 (0.50)	1.4 (1.4)	-0.90 (3.0)
Ref-C1-SD ³	2000-2010	-2.4 (0.53)	-1.6 (0.59)	1.4 (1.1)	-0.76 (3.0)
EmFix ³	2000-2010	1.3 (0.55)	1.5 (0.44)	2.1 (0.87)	0.96 (2.5)
AltEmis ³	2000-2010	0.71 (0.73)	0.74 (0.66)	3.8 (1.4)	1.1 (3.4)
<i>MOPITT</i>	2000-2010	-2.5 (0.64)	-1.8 (0.69)	-2.9 (1.8)	-1.4 (2.8)
<i>MOPITT</i>	2000-2014	-2.1 (0.41)	-1.7 (0.43)	-3.1 (1.1)	-1.4 (1.7)

¹10¹⁶ molec cm⁻² yr⁻¹

²1-sigma uncertainty given in parentheses

³Simulation results convolved with MOPITT averaging kernel and a priori

b. Correlation coefficient (r) with monthly MOPITT anomalies^{1,2}

	Years	E. USA	Europe	E. China	N. Hemisphere
G-Ref-C1	2000-2010	0.26	0.39	0.061	0.71
C-Ref-C1	2000-2010	0.23	0.36	0.18	0.62
Ref-C1-SD	2000-2010	0.43	0.51	0.39	0.73
EmFix	2000-2010	0.10	0.21	0.071	0.059
AltEmis	2000-2010	0.55	0.59	0.48	0.69

¹Correlations are calculated from the de-trended and de-seasonalized time series.

²Statistically significant correlations at the 95% confidence level are indicated in bold.

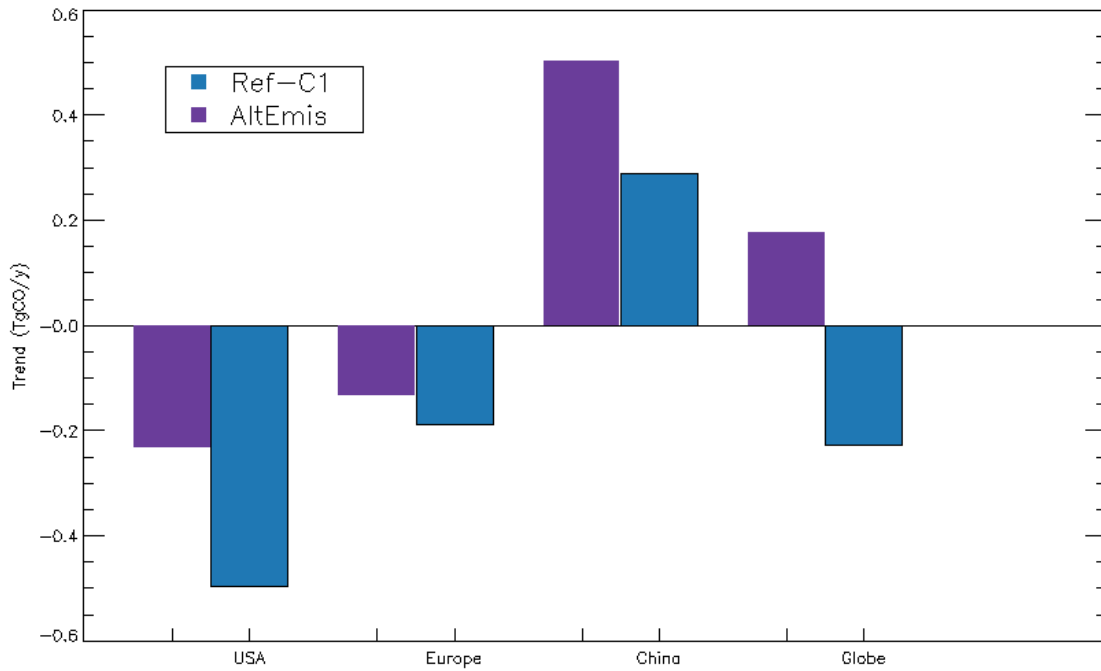


Figure 1: Trends in the CO emissions used in the Ref-C1 and Ref-C1-SD simulations (blue bars) and AltEmis simulation (purple bars) over 2000-2010 for the United States, Europe, China, and the world.

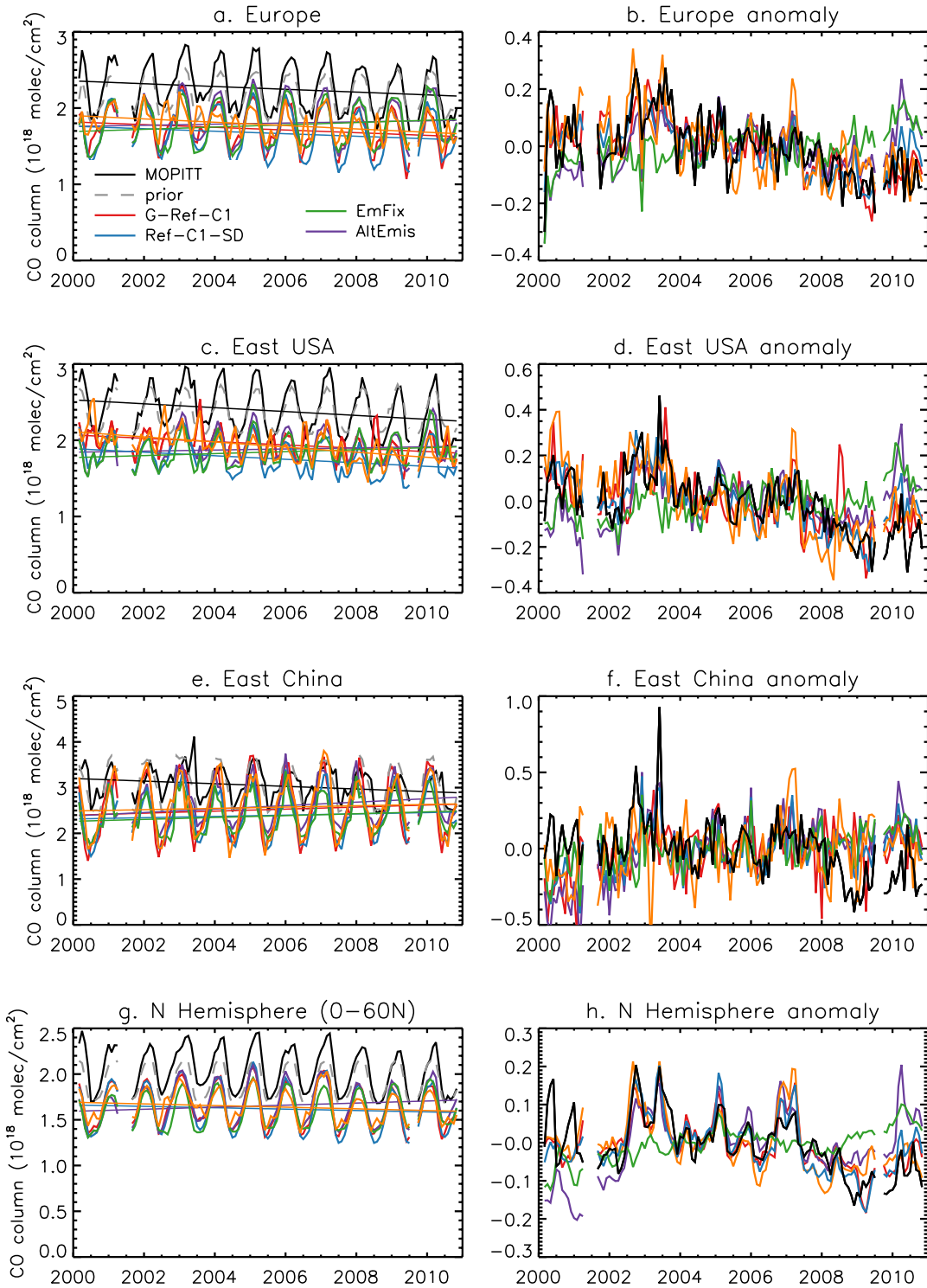


Figure 2: The time series and trends (left column) and de-seasonalized monthly anomalies (right column) of the CO column from MOPITT (black), the MOPITT a priori (gray), and simulated by G-Ref-C1 (red), Ref-C1-SD (blue), EmFix (green), C-Ref-C1 (orange), and AltEmis (purple) for 2000–2010. The regions shown are (a,b) Europe (0° – 60° N), (c,d) East USA (0° – 60° N), (e,f) East China (0° – 60° N), and (g,h) N Hemisphere (0° – 60° N).

15°E, 45°-55°N), (c,d) eastern U.S.A. (95°-75°W, 35°-40°N), (e,f) eastern China (110°-123°E, 30°-40°N), and (g,h) the northern hemisphere (0°-60°N).

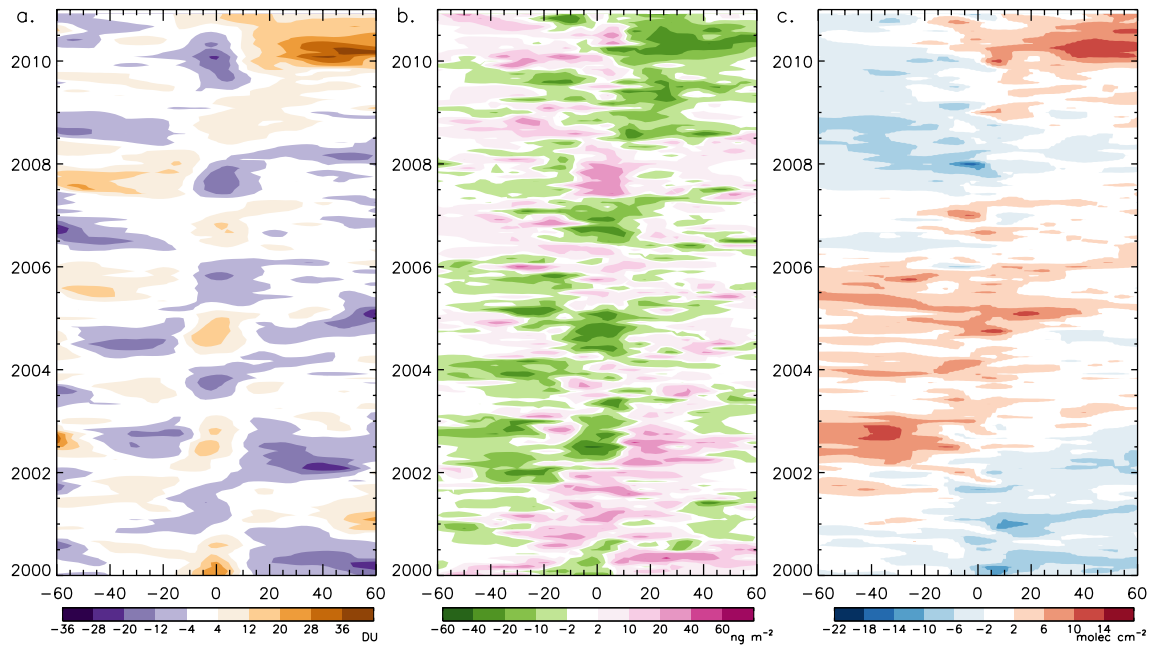


Figure 3: Deseasonalized monthly anomalies in the total ozone column (left), mean tropospheric OH (center), and CO column (right) from the EmFix simulation as a function of latitude and month.

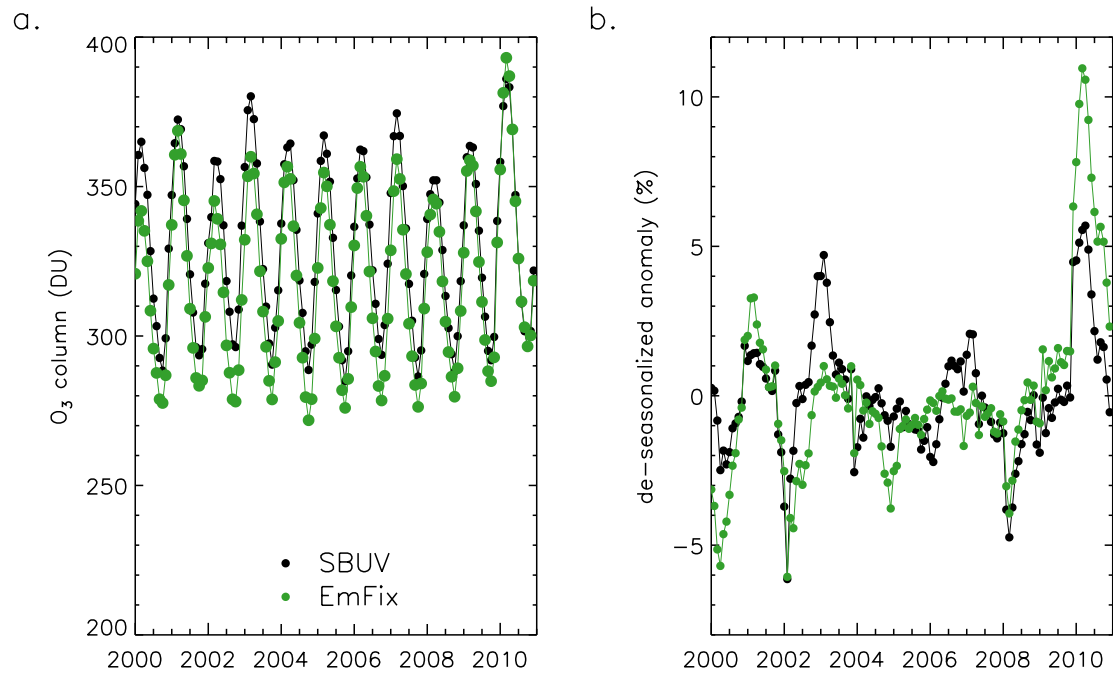


Figure 4: Monthly ozone column (a) and de-seasonalized ozone column anomaly (b) in SBUV data (black) and the EmFix simulation (green) for 30° - 60° N.

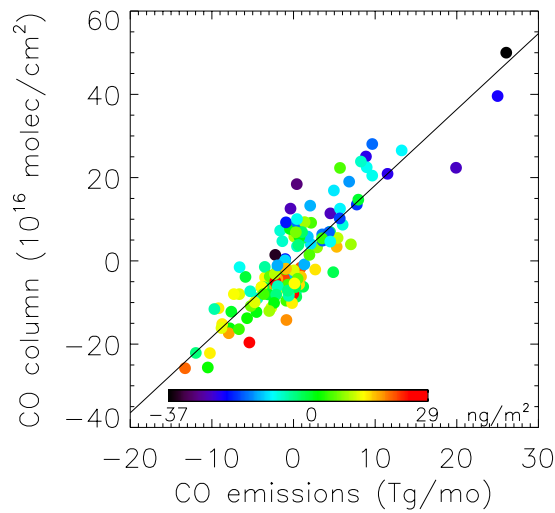


Figure 5: Monthly simulated CO column anomalies from the Ref-C1-SD simulation as a function of CO emissions for 10° S- 10° N. Colors indicate the simulated OH column anomaly for the given month.